Improving Damped Random Walk parameters for SDSS Stripe82 Quasars with Pan-STARRS1.

Krzysztof L. Suberlak,[1] Željko Ivezić,[1] and Chelsea MacLeod[2]

[1]*Department of Astronomy*
University of Washington
Seattle, WA 98195, USA
[2]*Harvard Smithsonian Center for Astrophysics*
60 Garden St, Cambridge, MA 02138, USA

ABSTRACT

We use the Panoramic Survey Telescope and Rapid Response System 1 Survey (Pan-STARRS1 or PS1) data to extend the Sloan Digital Sky Survey (SDSS) Stripe 82 quasar light curves. Combined datasets afford 15 year baselines for 9248 quasars, improving on previous studies using SDSS only. We make predictions on fidelity of DRW retrieval once ZTF and LSST data become available. We fit the light curves with Damped Random Walk (DRW) model, and correlate the DRW parameters - asymptotic variability amplitude SF_∞, and characteristic timescale τ, with quasar properties - black hole mass, bolometric luminosity, and redshift. We find that characteristic timescale τ is more strongly dependent on luminosity, and has a weaker dependence on black hole mass. The variability amplitude is less strongly dependent on the quasar luminosity.

1. INTRODUCTION

Quasars are inherently variable sources at the rms level of 0.2 mag. They are distant active galactic nuclei, harboring a supermassive black hole surrounded by a hot accretion disk. Although it is agreed upon that majority of optical emission stems from the accretion disk, the detailed origin of variability has been debated over the past 50 years (Sun et al. 2018 and references therein). Some favor a thermal origin of variability (Kelly et al. 2013), related to the propagation of inhomogeneities ("hot spots") in the disk (Dexter & Agol 2011; Cai et al. 2016), others suggested magnetically elevated disks (Dexter & Begelman 2019), or X-ray reprocessing (Kubota & Done 2018). Quasar light curves have been successfully described using the Damped Random Walk (DRW) model (Kelly et al. 2009; MacLeod et al. 2010; Kozłowski et al. 2010; Zu et al. 2011; Kasliwal et al. 2015), and the DRW parameters have been linked to the physical quasar properties. MacLeod et al. (2010) (M10) found correlations of the characteristic timescale

and variability amplitude to the black hole mass, and quasar luminosity.

Variability is also a classification tool, allowing to distinguish quasars from other variable sources that do not exhibit such stochastic variability pattern (MacLeod et al. 2011). Using the DRW parametrization, (MacLeod et al. 2011) found that DRW timescale and amplitude for QSO are order of magnitude different from stars. This is especially useful for selecting quasars in the intermediate redshift range (which overlaps the stellar locus in color-color diagrams - see Sesar et al. 2007; Yang et al. 2017). Variability has also been used to increase the completeness in measurements of Quasar Luminosity Function (see Ross et al. 2013; Palanque-Delabrouille et al. 2013; AlSayyad 2016; McGreer et al. 2013, 2018).

Due to its stochastic nature, the DRW process requires the light curve to be many times longer than the characteristic timescale for an unbiased parameter retrieval. The rule of thumb is that the light curve must be at least ten times longer than its characteristic timescale (Kozłowski et al. 2010; Kozłowski, Szymon 2017). For this reason some studies have restricted the probed redshift range, limiting the quasar sample to where one would expect only shorter timescales based on previous studies (Sun et al. 2018; Guo et al. 2017). Others have

Corresponding author: Krzysztof Suberlak
suberlak@uw.edu

suffered from short-baseline biases by employing single-survey data (Hernitschek et al. 2016). Thus by extending available quasar light curves we are able to better recover a wider range of DRW timescales, and probe a wider range of redshifts and black hole masses.

Almost a decade ago MacLeod et al. (2010) (hereafter M10) published their research using the SDSS Stripe 82 data, and new datasets (PS1,PTF,CRTS) have become available since that can extend the quasar light curves by almost 50% . Indeed, (Li et al. 2018) combined SDSS and Dark Energy Camera Legacy Survey (DECaLS) data, to provide a 15 year baseline, but by focusing on a large area to encompass as many quasars as possible (119,305 up to z=4.89) suffered from poor sampling which lends itself better to an ensemble structure function approach rather than direct light curve modeling. On the other hand, (Sánchez-Sáez et al. 2018) who employed optical data from QUEST-La Silla AGN variability survey, also used the Structure Function parametrization (amplitude of variability and the excess variance), because the light curve length (less than 5 years for 2435 quasars) excluded the possibility of unbiased retrieval of characteristic timescale.

This paper improves on the DRW parameters (Section 2) describing amplitude and characteristic timescale of Stripe82 quasars by extending the SDSS light curves for well-sampled Stripe82 with PanStarrs1 (PS1) data (Sections 3 and 4). We revisit trends between the DRW parameters and physical quasar properties, such as black hole mass, or bolometric luminosity (Section 5). We make predictions for fidelity of DRW parameter retrieval once ZTF and LSST data become available. In this work we adopt a ΛCDM cosmology with $h_0 = 0.7$ and $\Omega_m = 0.3$.

2. METHODS

2.1. DRW as a Gaussian Process

Damped Random Walk (OrnsteinUhlenbeck process) can be modeled as a member of a class of Gaussian Processes (GP). Each GP is described by a mean and a kernel - a covariance function that contains a measure of correlation between two points x_n, x_m, separted by Δt_{nm} (autocorrelation). For the DRW process, the covariance between observations of a source separated by Δt_{nm} is :

$$k(\Delta t_{nm}) = a \exp(-\Delta t_{tm}/\tau) \qquad (1)$$
$$= \sigma^2 \exp(-\Delta t_{tm}/\tau) \qquad (2)$$
$$= \sigma^2 ACF(\Delta t_{tm}) \qquad (3)$$

Here a or σ^2 is an amplitude of correlation decay as a function of t_{tm}, while τ is the characteristic timescale

over which correlation drops by $1/e$. For a DRW, the correlation function $k(\Delta t_{nm})$ is also related to the autocorrelation function ACF.

Not explicitly used in this paper, but of direct relevance to DRW modeling, is the structure function (SF). SF can be found from the data $\{m_i, t_i\}$ as the root-mean-squared of magnitude differences Δm calculated as a function of temporal separation Δt. SF is directly related to a DRW kernel $k(\Delta t_{nm})$:

$$SF(\Delta t) = SF_\infty(1 - \exp(-|\Delta t|/\tau))^{1/2} \qquad (4)$$

For quasars the SF follows approximately a power law: $SF \propto \Delta t^\beta$, and it levels out for large time lags Δt to a constant value of SF_∞. Note that $SF_\infty = \sqrt{2}\sigma$ in the above (also see MacLeod et al. (2012); Bauer et al. (2009); Graham et al. (2015) for an overview).

The likelihood is evaluated with celerite(Foreman-Mackey et al. 2017) - a fast GP solver that scales linearly with the number of data points $\mathcal{O}(N)$ thanks to an optimization that exploits the structure of covariance matrix for kernels that are a mixture of exponentials, such as a DRW kernel(Foreman-Mackey et al. 2018; Ambikasaran et al. 2015). The method employed is similar to that used by Rybicki & Press (1992); Kozłowski et al. (2010), M10 - like in previous work, we use a uniform prior on σ and τ. The main difference is that rather than adopting the Maximum A-Posteriori (MAP) as the 'best-fit' value for the DRW parameters, we find the expectation value of the marginalized log posterior. If the posterior space was a 2D Gaussian in σ, τ space, the expectation value would coincide with the maximum of the log posterior. However, due to non-Gaussian shape of the log posterior, the expectation value is a better estimate of σ and τ rather than MAP.

2.2. The impact of light curve baseline

K17 reports that one cannot trust any results of DRW fitting unless the light curve length is at least ten times longer than the characteristic timescale. We confirm these generic trends by repeating his simulation setup. We model 10 000 DRW light curves with fixed length (baseline) $t_{exp} = 8$ years, $SF_\infty = 0.2$ mag, SDSS or OGLE-like cadence, sampling over a range of input timescales. Given fixed baseline, this means exploring the parameter space of $\rho = \tau/t_{exp}$, $\rho \in \{0.01 : 15\}$. We simulate 100 light curves at each ρ.

To simulate observational conditions we add to the true underlying signal $s(t)$ a noise offset, $n(t)$. Like K17, we assume $n(t)$ to be drawn from a Gaussian distribution $\mathcal{N}(0, \sigma(t))$ with a width $\sigma(t)$, corresponding to the photometric uncertainty at the given epoch, $e(t)$) :
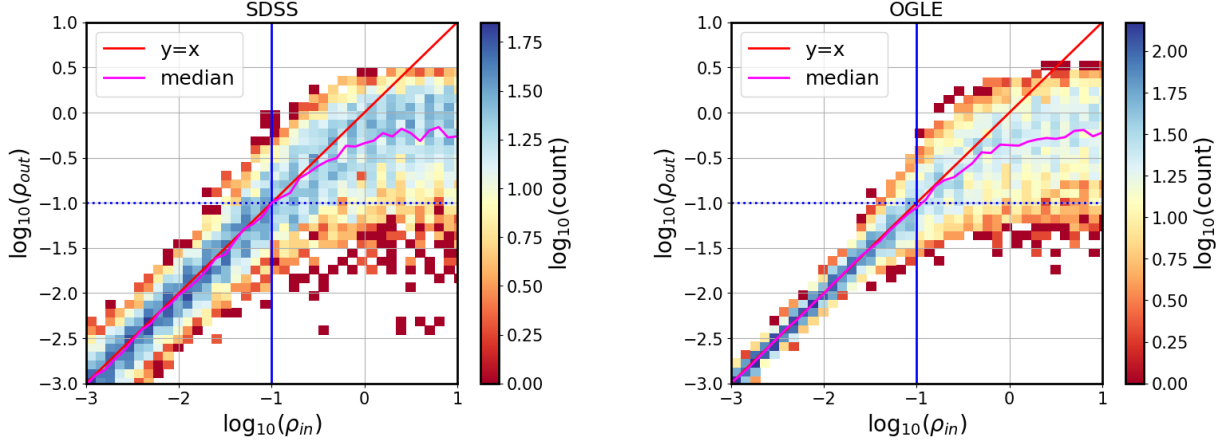
Figure 1. Probing the parameter space of $\rho = \tau/t_{exp}$, with a simulation of 10 000 light curves : 100 light curves per each of 100 ρ values spaced uniformly in logarithmic space between $\rho \in \{0.01 : 15\}$. Thus with the baseline t_{exp} set to 8 years, we sample a range of 100 input timescales, as in K17. Left panel shows the SDSS-like cadence with N=60 points, and the right panel OGLE-like cadence with N=445 points. The dotted horizontal and solid vertical lines represent $\rho = 0.1$, i.e. the baseline is ten times longer than considered timescale. The diagonal line is $y = x$, i.e. the line that would be followed if the recovered ρ (τ) was exactly the same as the input ρ (τ).

$$y(t) = s(t) + n(t) \tag{5}$$

The $s(t)$ is found by iterating over the array of time steps t. At each step, we draw a point from a Gaussian distribution, for which the mean and standard deviation are re-calculated at each timestep. Starting at t_0, the signal is equal to the mean magnitude, $s_0 = m$. After a timestep $\Delta t_i = t_{i+1} - t_i$, the signal s_{i+1} is drawn from $\mathcal{N}(loc, stdev)$, with :

$$loc = s_i e^{-r} + m \left(1 - e^{-r}\right) \tag{6}$$

and

$$stdev^2 = 0.5 \, SF_\infty^2 \left(1 - e^{-2r}\right) \tag{7}$$

where $r = \Delta t_i/\tau$, τ is the damping timescale, SF_∞ is the variability amplitude , and m the mean magnitude. This follows the formalizm in Kelly et al. (2009) (eqs. A4 and A5) as well as in MacLeod et al. (2010) (Sec. 2.2), and is equivalent to the setup of K17.

We adopt SDSS S82-like cadence with N=60 epochs, or OGLE-III like cadence with N=445 epochs. The errors are set by the adopted mean magnitudes, $r = 17$ and $I = 18$:

$$\sigma_{SDSS}^2 = 0.013^2 + \exp\left(2(r - 23.36)\right) \tag{8}$$
$$\sigma_{OGLE}^2 = 0.004^2 + \exp\left(1.63(I - 22.55)\right) \tag{9}$$

Fig. 1 confirms the findings of K17: recovered ρ becomes meaningless ('unconstrained') if the available DRW light curve baseline is not at least ten times longer

than the input timescale. It also means that by extending the baseline we can move from the biased region to the unbiased regime. Encouraged by this result, we extend the baselines of quasar light curves, and revisit relations studied by M10.

2.3. Departure from DRW?

The power spectral density (PSD) of the DRW process is:

$$P(f) = \frac{4\sigma^2\tau}{1 + (2\pi\tau f)^2} \tag{10}$$

(with $\sigma = SF_\infty/\sqrt{2}$, τ is the characteristic timescale, f is the frequency), so that $P(f) \propto f^{-2}$ at high frequencies $f > (2\pi\tau)^{-1}$, and levels to a constant value at lower frequencies(Kelly et al. 2014). This can be parametrized as $P(f) \propto f^{\alpha_h}$ at high frequencies (short timescales), and $P(f) \propto f^{\alpha_l}$ at low frequencies (long timescales), so that for a pure DRW process $\alpha_h = -2$ and $\alpha_l = 0$. Various opinions exist about the exact value of α_l and αh for accurate description of quasar variability, or more broadly speaking - AGN variability. For instance, Guo et al. (2017) using a low-redshift subset of S82 quasars finds that the low-frequency slope α_l should not be steeper than -1.3. Also, since short timescales are exquisitely probed by Kepler, (Aranzana et al. 2018) conducted the most extensive study of K2 AGN light curves to date, including 252 well-sampled quasars with a baseline of 80 days, and cadence of 30 mins. That study shows that while there is a range of PSD slopes from -1 to -3.2, the median of -2.2 is consistent with the DRW model. Furthermore, (Sun et al. 2018) found that the data quality of SDSS-like light curves is insufficient to distinguish

between CAR(1) and more complex models. Likewise, (Zu et al. 2013) using 223 I-band OGLE quasar light curves (baseline of $\approx$ 7 years, $\approx$ 570 epochs) considered whether different covariance functions (powered-exponential, Matèrn, Kepler-exponential, Pareto exponential - see Eqs.5,6,8,9 in Zu et al. 2013) may present a better fit, and found that while there may be small deviations, they are not significant enough to depart from a robust DRW description.

However, (Kozłowski, Szymon 2017) claims that based on Kozłowski (2016) and (Caplar et al. 2017), AGNs have PSD slopes $\alpha_h \leqslant -2$, which means that models assuming a DRW $\alpha_h = 2$ would result in decorrelation timescales biased low. It is currently not possible to distinguish between close-to-DRW and DRW processes for the S82 quasars because good sampling at both low frequencies (long timescales, white noise part), and high frequencies (short timescales, red / pink noise part)Kozłowski, Szymon (2017).

In the end, we follow the direction laid out in M10, Sec.4.4, which shows that while within S82 sampling assuming $\alpha_h = 2$ it is impossible to reliably distinguish between a $\alpha_l = 0$ and -1. A future study with appropriate cadence would be necessary to model each quasar individually with different α_l and α_h. We elect to use the DRW description ($\alpha_l = 0$, $\alpha_h = -2$) to allow a better comparison of our results with M10.

3. DATA

3.1. Surveys

We focus on THE data pertaining to a 290 deg^2 region of southern sky, repeatedly observed by SDSS between 1998 and 2008. Originally aimed at supernova discovery, objects in this area, known as Stripe82 (S82), were re-observed on average 60 times (see MacLeod et al. 2012 Sec. 2.2 for overview, and Annis et al. 2014 for details) . Availability of well-calibrated (Ivezić et al. 2007), long-baseline light curves spurred variability research (see Sesar et al. 2007). The catalog prepared by (Schneider et al. 2008) as part of DR9 contains 9258 spectroscopically confirmed quasars.

We extend the SDSS light curves with PanSTARRS (PS1) (Chambers 2011; Flewelling 2018), CRTS (Drake et al. 2009), and PTF (Rau et al. 2009) data. We find 9248 PS1 matches, 6455 PTF matches, and 7737 CRTS matches to SDSS S82 quasars. There are 6444 quasars with SDSS-PS1-PTF-CRTS data. Fig 2 depicts the baseline coverage of various surveys. Each survey uses a unique set of bandpasses and cadences : SDSS light curves contain near-simultaneous $\{u, g, r, i, z\}_{SDSS}$, and the others are non-simultaneous : $\{g, r, i, z, y\}_{PS1}$, $\{g, R\}_{PTF}$, V_{CRTS}.

3.2. Photometric offsets

We combine the photometry into a single 'master' bandpass. We choose SDSS r as the target since it has the best photometry, and we calculate color terms that afford transformation from other photometric systems to SDSS. We elect only to translate to SDSS r photometry from nearby filters : ($\{g, R\}_{PTF}$, $\{g, r, i\}_{PS1}$, V_{CRTS}).

Color terms are derived using SDSS standard stars catalog (Ivezić et al. 2007). We focused on 10% subset of randomly chosen stars from the catalog, and found CRTS (B.Sesar, priv.comm.), PS1 (from MAST http://panstarrs.stsci.edu) and PTF (IRSA PTF Object Catalog https://irsa.ipac.caltech.edu/) matches.

We consider the difference between the target (SDSS) and source (eg.PS1) photometry as a function of mean SDSS $(g - i)$ color :

$$m_{PS1} - m_{SDSS} = f(g - i) \qquad (11)$$

While Tonry et al. (2012) chose to spread the stellar locus with $(g - r)$ color, we prefer to use the $(g - i)$ color since it provides a larger wavelength baseline. Some authors (eg. Li et al. (2018)) allow $f(g-i)$ to be a higher-order polynomial, but since we limit the transformation to the region of $(g-i)$ space occupied by quasars (Fig. 3), we find that the linear fit is sufficient (see Fig. 4). Table 1 shows the offsets used to transform PS1, CRTS and PTF to SDSS r-band.

4. SIMULATIONS : LESSONS LEARNED

We simulate the theoretical improvement in the retrieved DRW parameters in combined light curves by generating long and well-sampled light curves, all with input $\tau = 575$ days, $SF_\infty = 0.2$ mag (the median of S82 distribution in M10). We then select SDSS, or SDSS-PS1 segments, sampling at the cadence corresponding to real light curves. We also predict the contribution of ZTF and LSST data (Fig. 5). For the ZTF 1-year segment (Spring 2019 ZTF Data Release will include data from 2018) we assumed 120 observations in ZTFg and ZTFr (every three nights), deriving the error model from the ZTF data for standard stars (Fig. 6). For the LSST 10-year segment (final LSST DR10 in 2031) we assumed 50 epochs per year, randomly distributed throughout the year, with the following error model:

$$\sigma_{LSST}(m)^2 = \sigma_{sys}^2 + \sigma_{rand}^2 \text{ (mag)}^2 \qquad (12)$$
$$\sigma_{rand}^2 = (0.04 - \gamma)x + \gamma x^2 \qquad (13)$$
$$x = 10^{0.4(m - m_5)} \qquad (14)$$

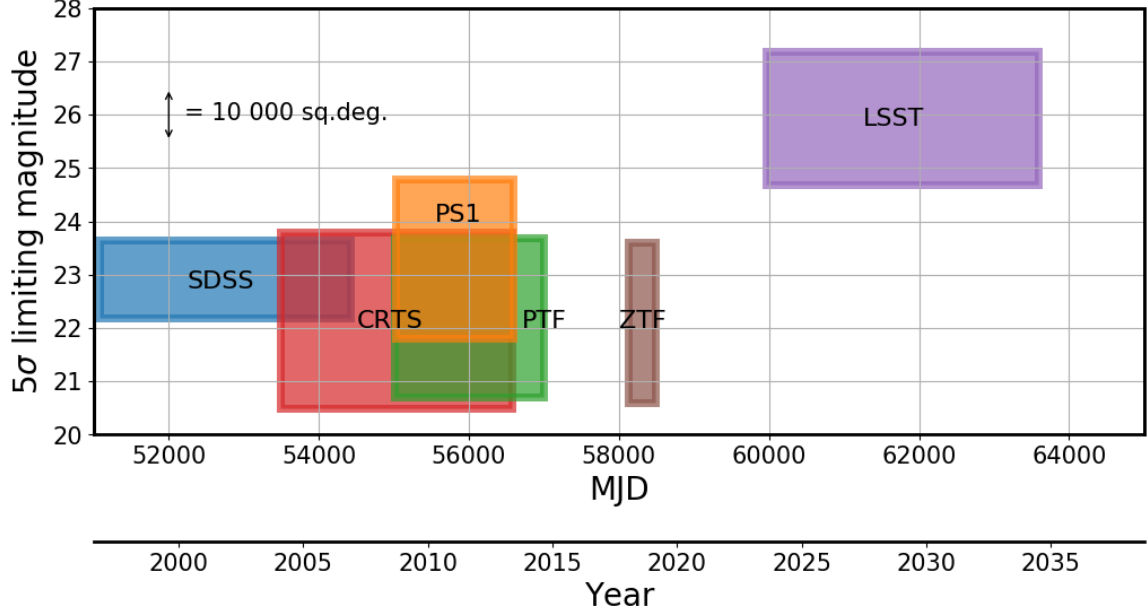with $\sigma_{sys} = 0.005$, $\gamma = 0.039$, $m_5 = 24.7$ (see Sec. 3.2 in Ivezić et al. (2019)).

Figure 2. An illustration of survey baseline, sky area covered, and depth. The width of each rectangle corresponds to the extent of light curves available (or simulated) for Stripe 82 quasars for each survey. For SDSS this means DR7; for CRTS DR2, PS1 DR2, PTF DR2, ZTF year 2018, and LSST the full 10-year survey. The lower edge of each rectangle corresponds to the 5σ limiting magnitude (SDSS r, PS1 r, PTF R, ZTF r, LSST r, CRTS V). The vertical extent corresponds to the total survey area (for SDSS, up to and including DR15). Note how PS1 and PTF extend the baseline of SDSS by approximately 50%, and how inclusion of LSST triples the SDSS baseline. For reference, the area covered by LSST is 25000 sq.deg., which corresponds to 60% of the sky. The whole sky has an area of 4π steradians (41253 sq.deg.).

To mirror observational conditions we add to the true underlying DRW signal a Gaussian noise, with variance defined by photometric uncertainties for corresponding surveys. Given the noise properties of each survey (Fig. 7), we found that relatively large uncertainties of CRTS and PTF segments introduced less improvement in recovery of DRW parameters, given that similar baseline is already covered by the PS1 data. We further found that inclusion of ZTF data for 2018 would not significantly change our results. Inclusion of PS1 data with its excellent photometry (as compared to ZTF or PTF) is the best improvement over existing SDSS results. In the future (after more data has been assembled and recalibrated) ZTF will help, but not as dramatically as LSST (see Fig. 8). For this reason we found that using only SDSS-PS1 portion is the best tradeoff between adding more baseline vs introducing more uncertainty with noisy data. Fig. 5 illustrates of the simulated light curve.

As we found earlier, extending the light curve baseline decreases the bias in the retrieved DRW parameters (Fig. 1). For light curves that simulate the extension of SDSS with PS1, ZTF, LSST segments, Figs. 8 and 9 show that this is indeed the case: as make light curves longer, the retrieved τ and SF_∞ become more centered on the input value.

5. RESULTS: FITTING SDSS-PS1 WITH CELERITE

We have extended the baseline of Stripe82 quasars by adding to SDSS r-band data the PS1 g,r,i data, transformed into common SDSS r-band. As the variability originates in the accretion disk, we shift all timescales to quasar rest frame : $\tau_{\mathrm{RF}} = \tau_{\mathrm{OBS}}/(1 + z)$.

We first show that our results are consistent with M10 when using only the SDSS r-band : on Fig. 10) the distributions of τ, SF_∞ from M10 (red) and our results (blue) coincide. Furthermore, when comparing object-by-object M10 to our SDSS-only results we find a very good agreement - histograms on Fig. 11 are peaked around 0.

5.1. *Rest-frame Wavelength Correction*

Prior to looking for correlations with physical quantities (black hole mass, luminosities, redshifts), we correct τ and SF_∞ for wavelength dependence using formulae from M10. Since quasars are at different redshifts, the same observed band would probe a different rest-frame wavelength λ_{RF} for each quasar. We find that the power law employed by M10:

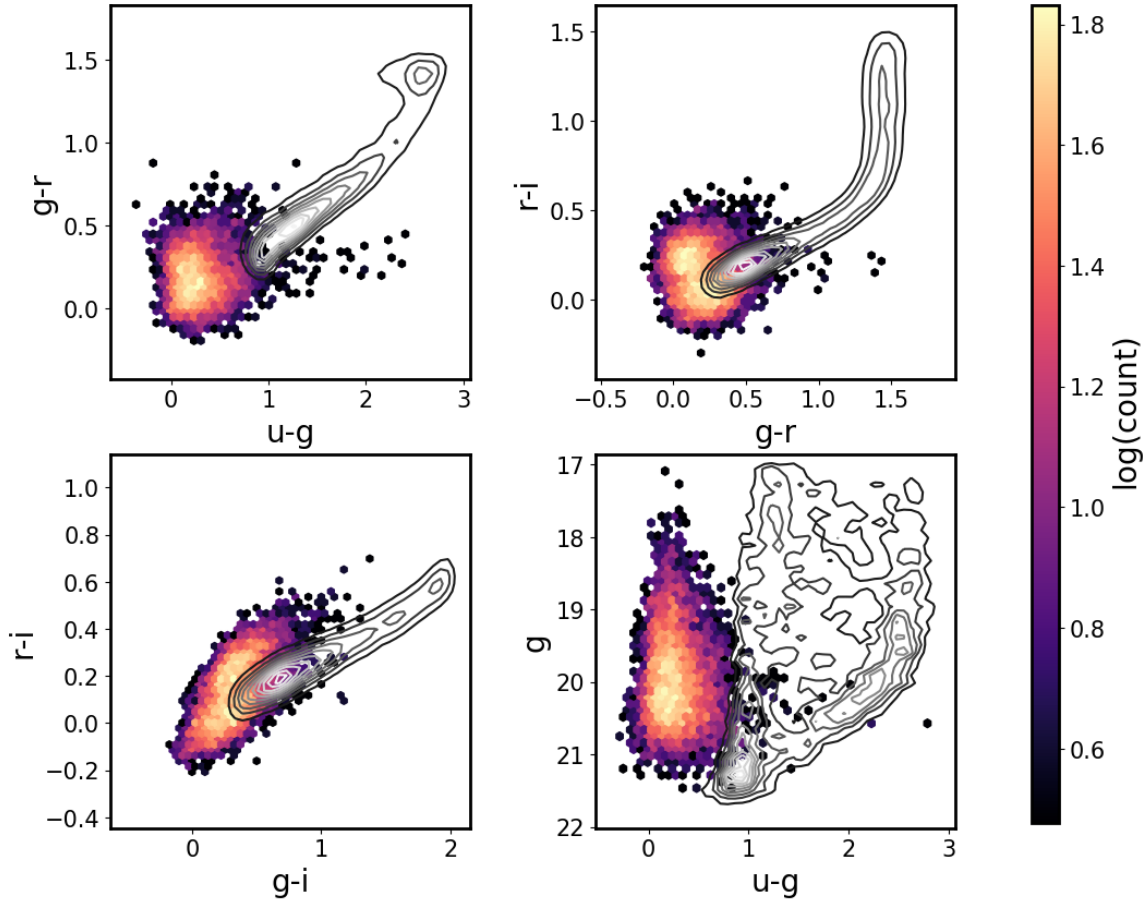$$f \propto \left(\frac{\lambda_{RF}}{4000\mathring{A}}\right)^{B} \tag{15}$$

Figure 3. Regions occupied in color-color space by S82 quasars (colors) and standard stars (contours) (Schneider et al. 2010). We show only 10 000 randomly chosen stars from the full 1 mln + standard stars catalog Ivezić et al. 2007. We limit the offset to SDSS $-0.5 < (g - i) < 1..$ Quasars also overlap other variable sources (eg. RRLyrae), not shown on this illustration Sesar et al. 2007.

together with the fit coefficients $B = -0.479$ and 0.17 for SF_∞ and τ, respectively, are adequate for our combined SDSS r-band results, as shown on Fig. 12 .

5.2. *Trends with Luminosity, Black Hole Mass, and Redshift*

Here we examine the main scientific results: correlations between variability parameters $(\tau, SF\infty)$, and the physical properties of quasars: absolute i-band magnitude M_i, and black hole mass M_{BH}.

First, we consider the selection effects that are inherent to the quasar distribution. Fig. 13 shows the distribution of quasars as a function of redshift z, i magnitude M_i, and black hole mass M_{BH}. For instance, the trend of increasing redshift with M_i on the upper left panel is due to the fact that quasars have to be brighter to be included in the survey at increasing distances.

As explained in (Shen et al. 2008, 2011), the most common approach to estimate quasar black hole mass is to assume that the broad-line region (BLR) is virialized, so that the continuum luminosity can be used as a proxy

for the BLR radius, and the width of the broad emission lines (or line dispersion) is used to compute the virial velocity. The most commonly used, calibrated emission lines, that are available across different redshifts, are broad Hα, Hβ, Mg II, and C IV (Vestergaard 2002).

There are various available catalogs of quasar properties : redshift, absolute i-band luminosity, black hole mass. Usually the first quasar catalog releases basic properties such as redshift and photometry (eg. Schneider et al. 2007, 2010, and then more involved studies derive black hole masses and bolometric luminosities (eg. Shen et al. 2008, 2011). This is also the case for more recent work: once (Pâris et al. 2017) released SDSS DR12 Quasar Catalog (DR12Q), (Kozłowski, Szymon 2017) followed by estimating from photometry the monochromatic luminosities, and deriving black hole masses, and (Chen et al. 2018) added a detailed analysis of continuum luminosities in the Hα, Hβ regions for low-redshift quasars. Using the spectra from Chinese LAMOST survey (Dong et al. 2018) also sought to estimate virial
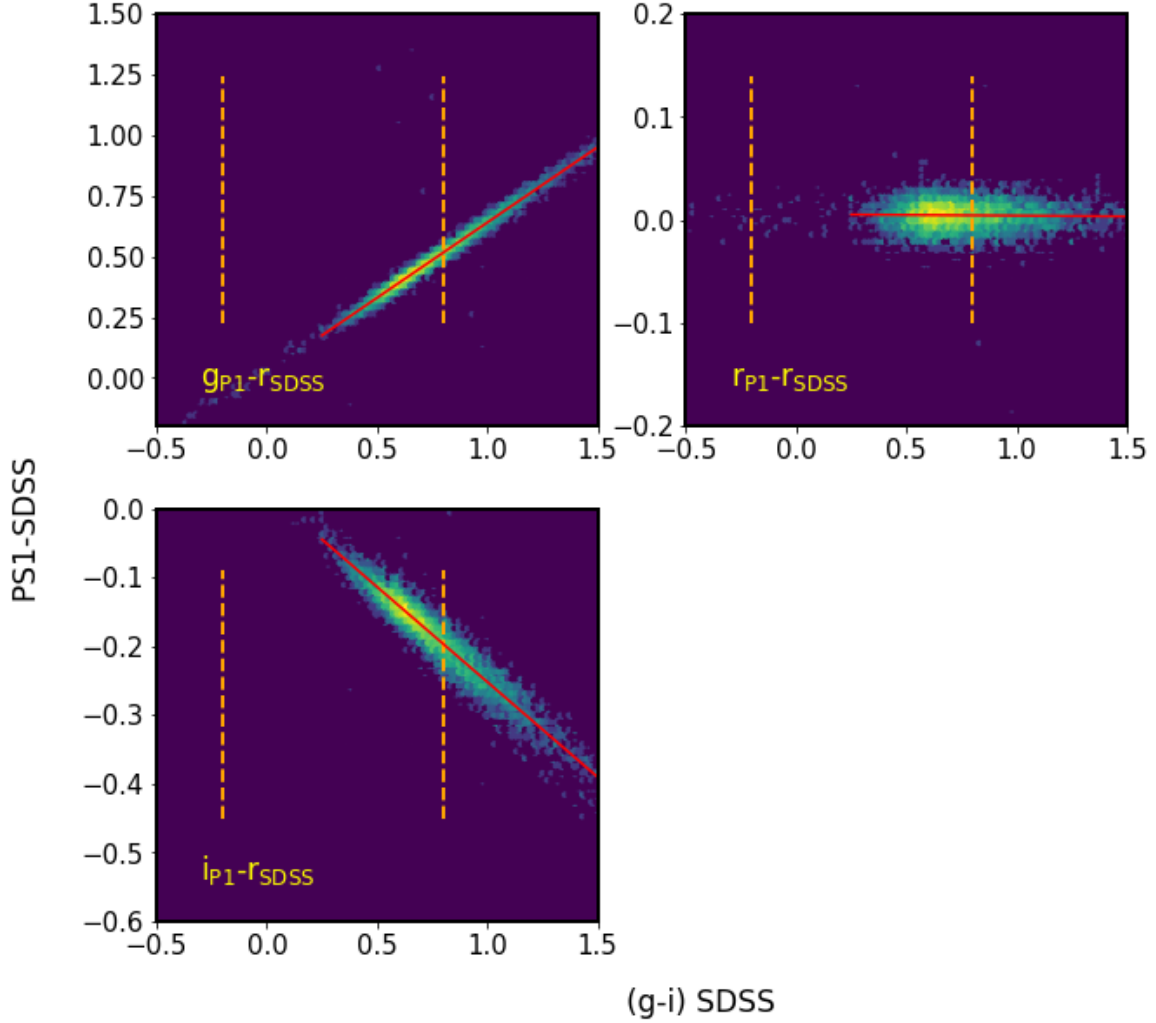
Figure 4. The SDSS-PS1 offsets. We plot only bright stars where SDSS $r < 19$, and that fulfill mErr * sqrt(Nobs) ¡ 0.03 . Each panel includes about 6000 standard stars. Vertical dashed lines mark the region in the SDSS color space occupied by quasars (see Fig. 3), used to fit the stellar locus with a polynomial.

black hole masses, and the results while consistent with (Shen et al. 2011), suffered from necessity to peg the non-calibrated spectra to SDSS photometry which was taken at a different epoch. For sources variable at ̃0.2 mag level, such as quasars, the ideal is to use single-epoch calibrated spectra to estimate continuum luminosity, and find virial black hole masses using relationships based on the monochromatic fluxes and broad line widths. Even though Pâris et al. (2018) DR14Q is the most recent catalog, like (Pâris et al. 2017) it lacks black hole masses and bolometric luminosities, and (Kozłowski, Szymon 2017) (henceforth K17) bases his analysis on a SDSS photometry as a proxy for monochromatic luminosities rather than directly from the spectra. Of all available catalogs, (Shen et al. 2011) provides the best to date measurements of quasar black hole masses

and monochromatic luminosities, based directly on the single-epoch spectra, and is therefore our choice.

The absolute i-band magnitude M_i is a good proxy for the bolometric luminosity (see Shen et al. 2008, Fig.2). M_i is derived from the observed i-band magnitude, by correcting for Galactic extinction, and K-correcting for the fact that at different redshifts different portions of the spectral energy distribution are observed by the telescope filter bandpass. Historically termed K-correction (Oke & Sandage 1968), $K(z)$ is defined as $m_{intrinsic} = m_{observed} - K(z)$. In the early 2000s the standard was to K-correct to redshift 0, but as (Richards et al. 2006) pointed out, since the distribution of quasars peaks at redshift 2, for most quasars K(z=0) required shifting the observed spectrum into the far infrared. The procedure was to correct separately for the continuum and emission line contributions, assum-
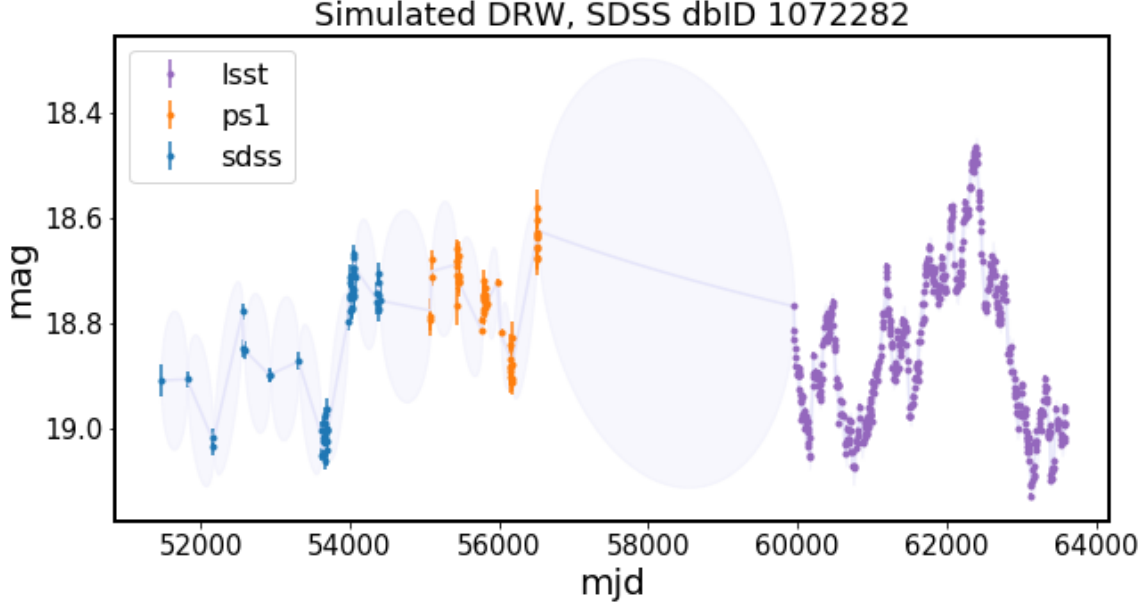
Figure 5. Simulated DRW process sampled at the real cadence of SDSS, PS1 segments for quasar SDSSdbID=1072282, adding the simulated LSST segment. The well-sampled true DRW signal was first sampled at SDSS-PS1-LSST cadences, and then Gaussian offset was added to each point to simulate observational noise.
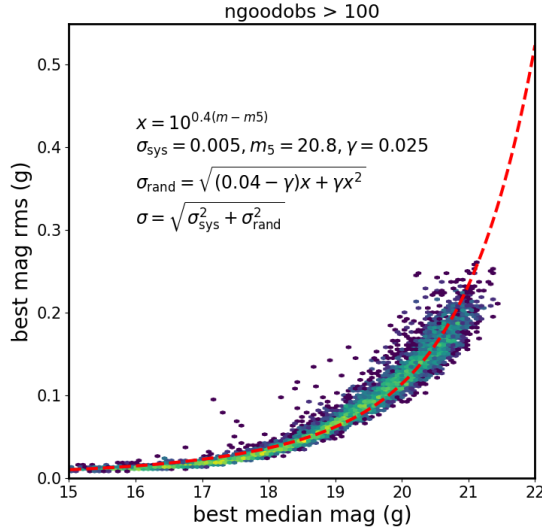

Figure 6. The rms spread as a function of magnitude for ZTF non-variable stars with over 100 observations. We over-plot the functional describing the adopted error model (after Ivezić et al. 2019). Properties of ZTF photometric uncertainties are largely similar to the PTF uncertainties.

Figure 7. Distribution of median photometric uncertainties (colloquially called 'errors') in combined r-band real light curves. This shows that the PTF and ZTF segments have much larger errors than SDSS, PS1. This is the reason for using only SDSS-PS1 part of the combined light curve.

ing a particular spectral shape (eg. power law $f_\nu \propto \nu^\alpha$, with $\alpha = -0.5$ - see Schneider et al. 2010; Vanden Berk et al. 2001; Richards et al. 2006). This introduced large error if the assumed spectral shape $\alpha = -0.5$ was far from the real spectral index. In early 2010s the standard started to shift towards K-correcting to redshift 2 (following Richards et al. 2006; Wisotzki 2000; Blanton et al. 2003), and including custom qusasar spectral

shapes, as we see eg. in the catalog of (Shen et al. 2011). Thus in this study we use the absolute i-band magnitude K-corrected to z=2: $M_i(z = 2)$ from (Shen et al. 2011).

We show on Fig. 14 τ and SF_∞ as a function of absolute magnitude M_i, redshift z, and black hole mass M_{BH}. We investigate these correlations in more detail fitting to f is τ_{RF} or SF_∞ a power law :

$$\log_{10} f = A + B \log_{10}\left(\lambda_{RF}/4000\text{Å}\right) + C(M_i + 23) + D \log_{10}\left(M_{BH}/10^9 M_\odot\right) \quad (16)$$

M10 fitted this power law independently to each of the five SDSS bands, reporting the band-averaged coefficients. Fig. 15 shows the example of posterior sam-
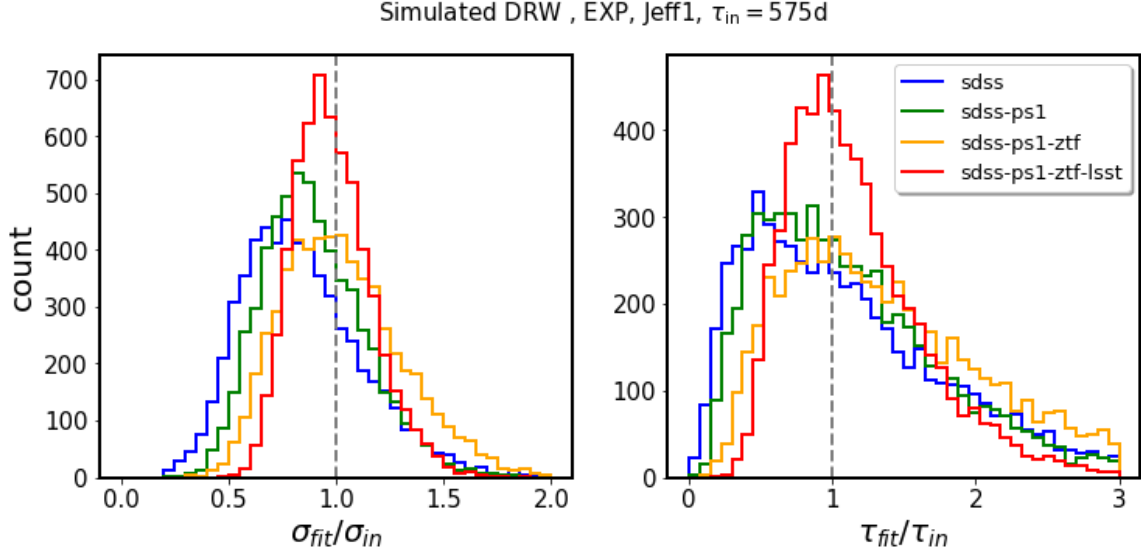
Simulated DRW , EXP, Jeff1, $\tau_{in} = 575d$

Figure 8. Retrieved τ and σ parameters for simulated LCs.

ples for $f = SF_\infty$ correlating the M10 SDSS ugriz data against an updated quasar catalog of (Shen et al. 2011).

Because we use the combined r-band data, we compare our results to M10 SDSS r-band only. We have already shown consistency of object-by-object results when using only SDSS segment in Figs. 10 and 11. Now we show that the trends recovered using SDSS-only portions are also consistent with M10. Fig. 17 shows the results for $f = SF_\infty$ - we find that there is a larger dependence of variability amplitude on quasar luminosity, but smaller dependence on black hole mass. Fig. 16 concerns the τ, which appears to be less correlated with both quasar luminosity and black hole mass.

5.3. *Comparison with other studies*

Sun et al. (2018) using 1000 low-z S82 QSO finds that variability amplitude is correlated with the inverse of bolometric luminosity, and suggests that since $\hat{\sigma}$ is so well related to L_{bol}, perhaps we could use the $\hat{\sigma} - L_{bol}$ relation to derive L_{bol} without assuming any cosmological models.

In principle any tight correlation between the variability parameters and physical properties of quasars could be used to infer eg. black hole mass or bolometric luminosity given only the optical time-series. In the era of large synoptic surveys (PS1, ZTF,LSST), this could provide additional information about quasars for which it will be impractical to obtain a spectrum (Sánchez-Sáez et al. 2018).

X-ray reprocessing is also consistent with the dependence of $\hat{\sigma}$ on the FeII strength, $R_{\rm FeII}$ (the ratio of the equivalent width of FeII between $4435 - 4685$ $\mathring{A}$ and Hβ) studied by (Sun et al. 2018). They chose $R_{\rm FeII}$, a proxy

for Eddington ratio, because it was found by (**?**), (**?**) to be anticorrelated with M_{BH}

Variability amplitude - Eddington ratio relation has been studied by

5.4. *Alternative method to estimate black hole masses*

In an absence of time-series for a quasar, an attractive alternative method to estimate black hole masses is presented by (Kozłowski 2015). Broad-band AGN photometry can be translated into monochromatic fluxes in the vicinity of the reverberating lines (Hβ 5100 $\mathring{A}$, Mg II at 3000 $\mathring{A}$, and C IV at 1350 $\mathring{A}$, Kozłowski 2015), which in turn can be used to estimate the virial black hole mass :

$$M_{BH} = \frac{fR\Delta V^2}{G} \qquad (17)$$

where f is a constant of order unity, R is the size of the Broad Line Region (estimated from emission-line lag Δt as $R = c\Delta t$), ΔV is the emission line width, G gravitational constant. From reverberation mapping studies we know that continuum luminosity L is related to the size of the BLR region as $R \propto L^\gamma$ (Vestergaard & Peterson 2006), with γ very close to $1/2$ (eg. Bentz et al. 2009 finds from RM studies $\gamma = 0.519 \pm 0.06$). Thus we obtain that $R\Delta V^2 \propto L^\gamma \Delta V^2 \equiv \mu$, and the black hole mass is a simple function of line width measurement and continuum luminosity :

$$\log M_{BH} = \log \mu + a \qquad (18)$$

This is also seen eg. in more recent study by (Shen et al. 2018) of the SDSS Reverberation Mapping sample.
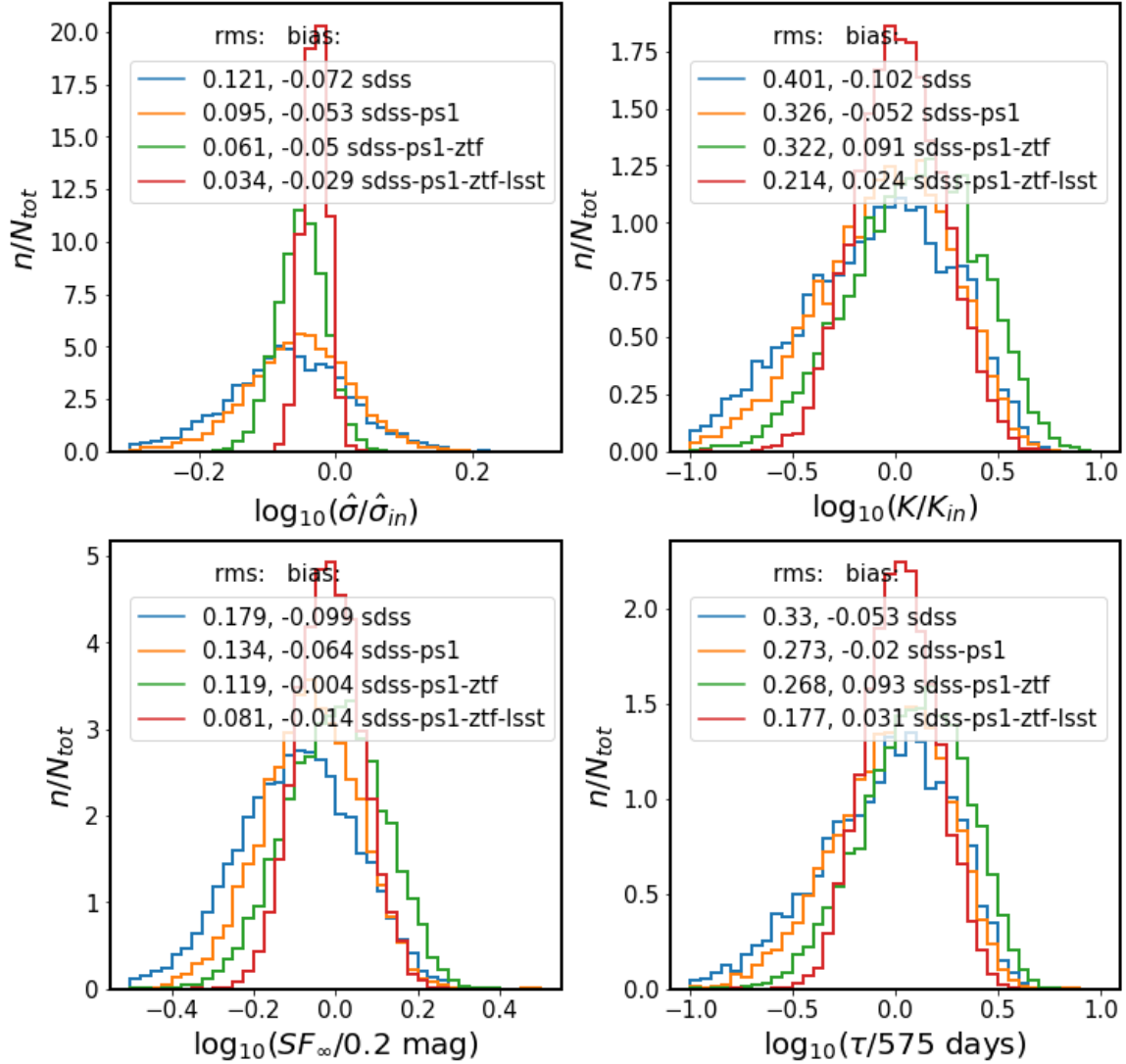
Figure 9. Comparison of retrieved parameters in relation to input parameters, shown as Fig.18 in MacLeod et al. (2011)

Ideally one would obtain a quasar spectrum to directly measure ΔV and L, and use Eq.18 to estimate the black hole mass. In the era of LSST, with an order of magnitude increase in the number of known quasars, spectroscopic follow-up of all is not feasible, but as long as the broad-band photometry is available, (Kozłowski 2015)

method (also applied to SDSS Quasar Data Release 12, see Kozłowski 2017) presents an attractive alternative to the variability-based black hole mass estimates.

6. CONCLUSIONS

REFERENCES

AlSayyad, Y. 2016, PhD thesis, University of Washington.
http://hdl.handle.net/1773/37020

Ambikasaran, S., Foreman-Mackey, D., Greengard, L.,
Hogg, D. W., & O'Neil, M. 2015, IEEE Transactions on
Pattern Analysis and Machine Intelligence, 38,
doi: 10.1109/TPAMI.2015.2448083

Annis, J., Soares-Santos, M., Strauss, M. A., et al. 2014,
ApJ, 794, 120, doi: 10.1088/0004-637X/794/2/120

Aranzana, E., Körding, E., Uttley, P., Scaringi, S., &
Bloemen, S. 2018, MNRAS, 476, 2501,
doi: 10.1093/mnras/sty413

Bauer, A., Baltay, C., Coppi, P., et al. 2009, ApJ, 696,
1241, doi: 10.1088/0004-637X/696/2/1241

Bentz, M. C., Peterson, B. M., Netzer, H., Pogge, R. W., &
Vestergaard, M. 2009, ApJ, 697, 160,
doi: 10.1088/0004-637X/697/1/160
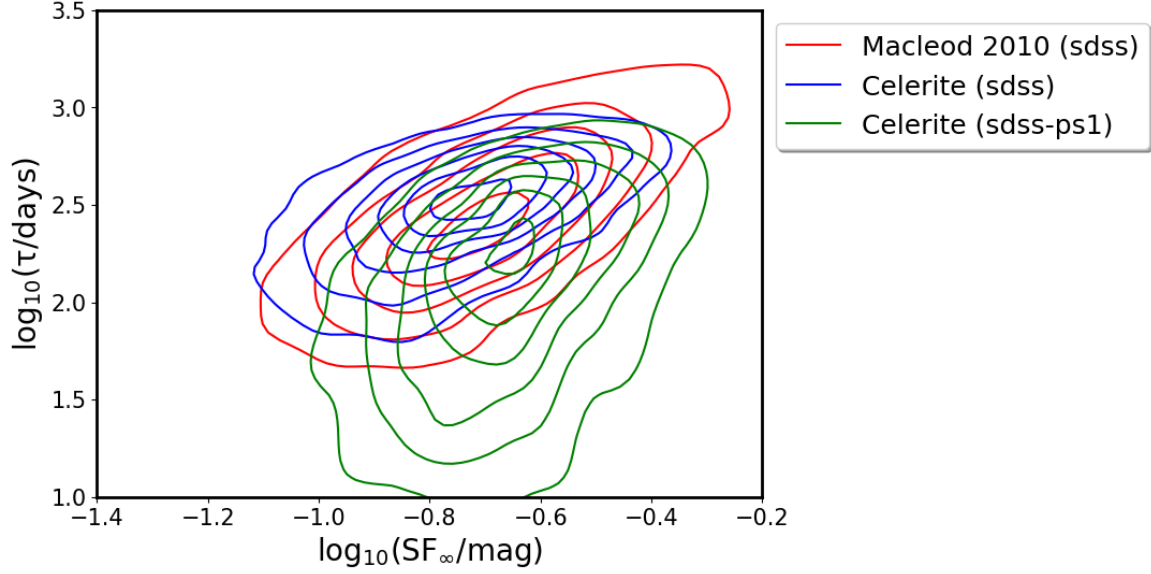
Figure 10. Comparing the rest-frame timescales τ, and asymptotic variability amplitudes SF_∞, for M10 SDSS r-band, and combined SDSS and PS1 data.
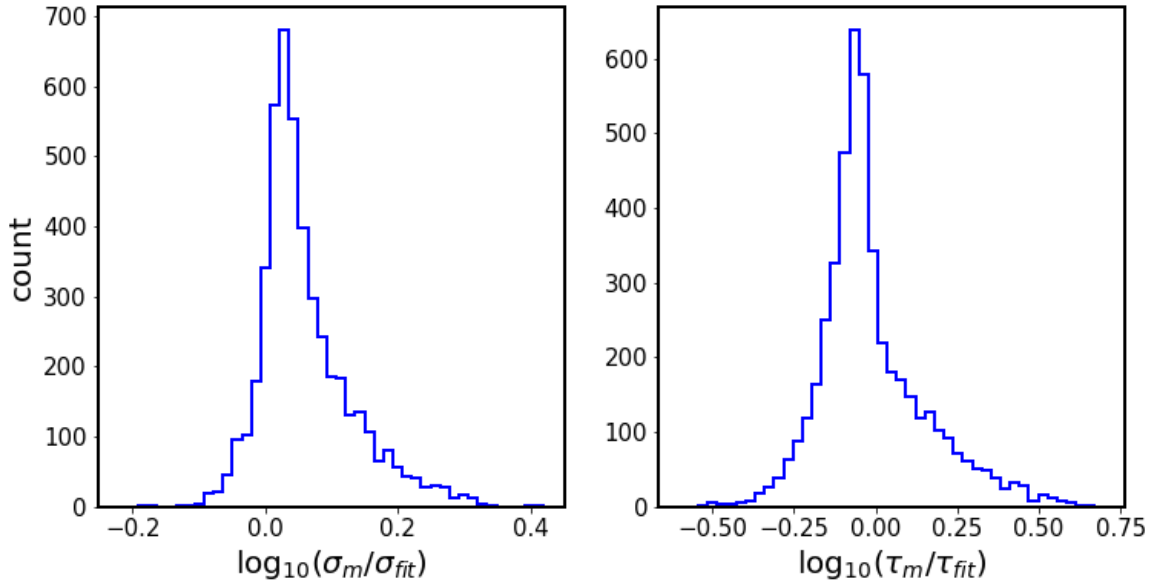
Figure 11. Plot comparing results for SDSS r-band fitting of M10 (σ_m, τ_m), and current results for SDSS r-band using Celerite $(\sigma_{fit}, \tau_{fit})$.

Blanton, M. R., Lin, H., Lupton, R. H., et al. 2003, AJ, 125, 2276, doi: 10.1086/344761

Cai, Z.-Y., Wang, J.-X., Gu, W.-M., et al. 2016, ApJ, 826, 7, doi: 10.3847/0004-637X/826/1/7

Caplar, N., Lilly, S. J., & Trakhtenbrot, B. 2017, ApJ, 834, 111, doi: 10.3847/1538-4357/834/2/111

Chambers, K. C. 2011, in Bulletin of the American Astronomical Society, Vol. 43, American Astronomical Society Meeting Abstracts #218, 113.01

Chen, Z.-F., Pan, D.-S., Pang, T.-T., & Huang, Y. 2018, ApJS, 234, 16, doi: 10.3847/1538-4365/aa9d90

Dexter, J., & Agol, E. 2011, ApJL, 727, L24, doi: 10.1088/2041-8205/727/1/L24

Dexter, J., & Begelman, M. C. 2019, MNRAS, 483, L17, doi: 10.1093/mnrasl/sly213

Dong, X. Y., Wu, X.-B., Ai, Y. L., et al. 2018, AJ, 155, 189, doi: 10.3847/1538-3881/aab5ae

Drake, A. J., Djorgovski, S. G., Mahabal, A., et al. 2009, ApJ, 696, 870, doi: 10.1088/0004-637X/696/1/870
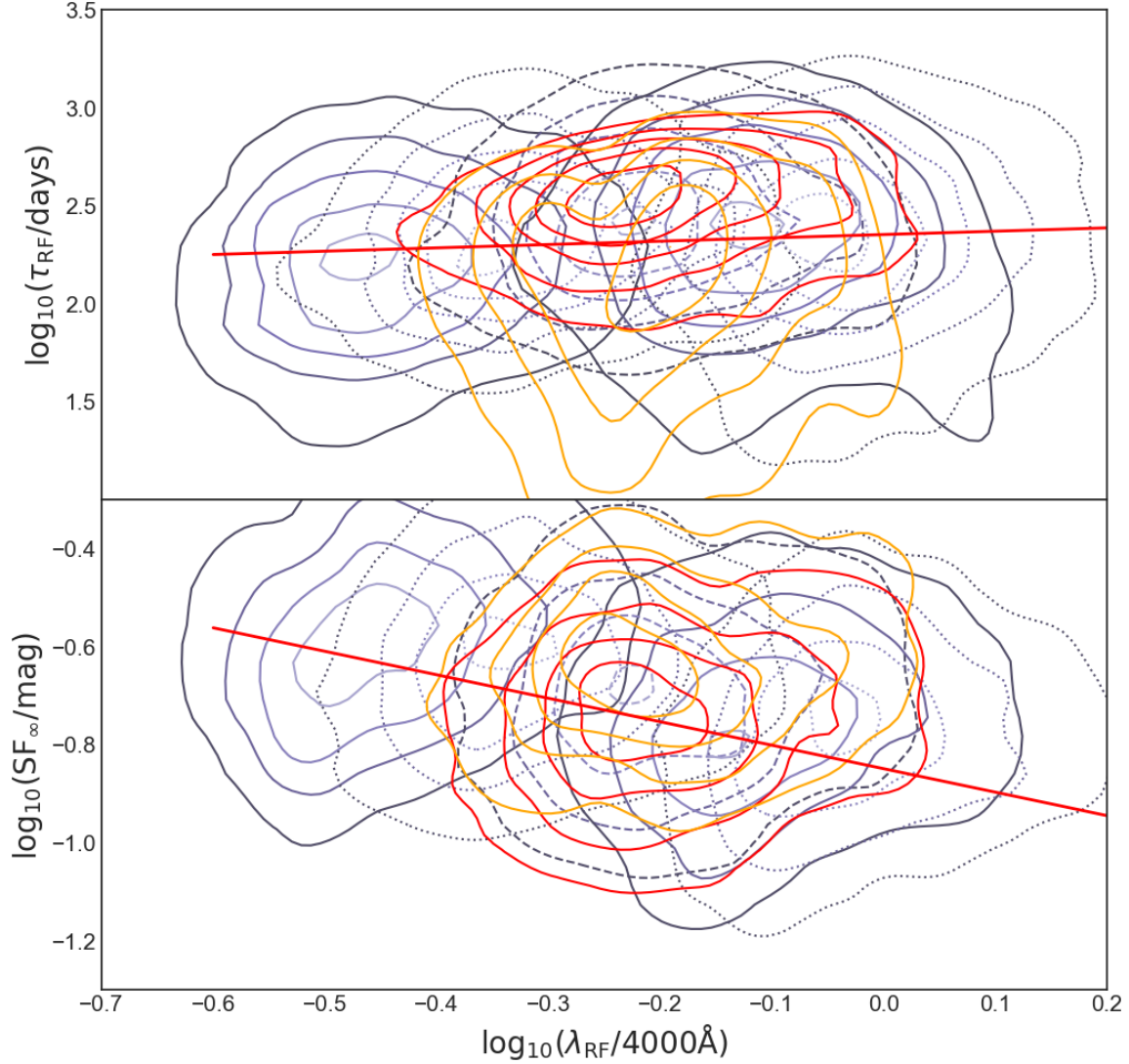
Figure 12. Rest-frame timescale τ (top panel), and asymptotic structure function SF_∞ (bottom panel), as a function of rest-frame wavelength λ_{RF}. The background contours show M10 SDSS $ugriz$ data, and the foreground contours denote our results using SDSS (red) and SDSS-PS1 (orange) segments. The red line indicates the best-fit power law to M10 data, with $B = 0.17$ an -0.479 for τ_{RF}, and SF_∞, respectively.

Flewelling, H. 2018, in American Astronomical Society Meeting Abstracts, Vol. 231, American Astronomical Society Meeting Abstracts 231, 436.01

Foreman-Mackey, D., Agol, E., Angus, R., & Ambikasaran, S. 2017, ArXiv e-prints.
https://arxiv.org/abs/1703.09710

Foreman-Mackey, D., Bernhard, J., Hoyer, S., Walker, S., & Angus, R. 2018, dfm/george: george v0.3.1,
doi: 10.5281/zenodo.1137793.
https://doi.org/10.5281/zenodo.1137793

Graham, M. J., Djorgovski, S. G., Stern, D., et al. 2015, Nature, 518, 74, doi: 10.1038/nature14143

Guo, H., Wang, J., Cai, Z., & Sun, M. 2017, ApJ, 847, 132, doi: 10.3847/1538-4357/aa8d71

Hernitschek, N., Schlafly, E. F., Sesar, B., et al. 2016, The Astrophysical Journal, 817, 73

Ivezić, Ž., Smith, J. A., Miknaitis, G., et al. 2007, AJ, 134, 973, doi: 10.1086/519976

Ivezić, Ž., Kahn, S. M., Tyson, J. A., et al. 2019, ApJ, 873, 111, doi: 10.3847/1538-4357/ab042c

Kasliwal, V. P., Vogeley, M. S., & Richards, G. T. 2015, MNRAS, 451, 4328, doi: 10.1093/mnras/stv1230

Kelly, B. C., Bechtold, J., & Siemiginowska, A. 2009, The Astrophysical Journal, 698, 895

Kelly, B. C., Becker, A. C., Sobolewska, M., Siemiginowska, A., & Uttley, P. 2014, ApJ, 788, 33,
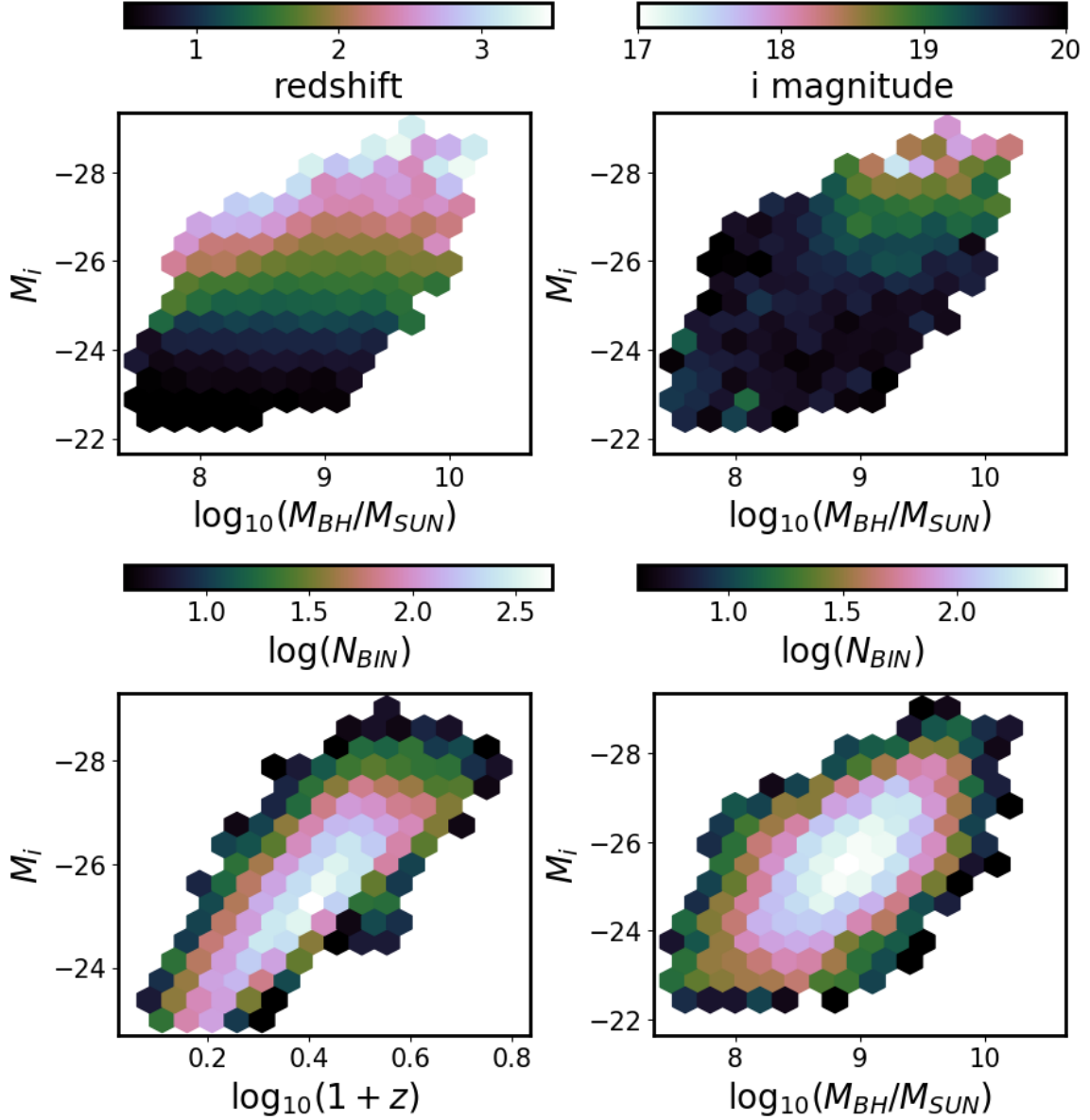doi: 10.1088/0004-637X/788/1/33

Figure 13. Distribution of quasars as a function of redshift, observed i-band magnitude, absolute i-band magnitude (K-corrected to z=2), and virial black hole mass. All quantities from (Shen et al. 2011).

Kelly, B. C., Treu, T., Malkan, M., Pancoast, A., & Woo, J.-H. 2013, ApJ, 779, 187, doi: 10.1088/0004-637X/779/2/187

Kozłowski, S. 2015, AcA, 65, 251. https://arxiv.org/abs/1504.05960

Kozłowski, S. 2016, MNRAS, 459, 2787, doi: 10.1093/mnras/stw819

Kozłowski, S. 2017, ApJS, 228, 9, doi: 10.3847/1538-4365/228/1/9

Kozłowski, S., Kochanek, C. S., Udalski, A., et al. 2010, ApJ, 708, 927

Kozłowski, Szymon. 2017, A&A, 597, A128, doi: 10.1051/0004-6361/201629890

Kubota, A., & Done, C. 2018, MNRAS, 480, 1247, doi: 10.1093/mnras/sty1890

Li, Z., McGreer, I. D., Wu, X.-B., Fan, X., & Yang, Q. 2018, ApJ, 861, 6, doi: 10.3847/1538-4357/aac6ce

MacLeod, C. L., Ivezić, Ž, Kochanek, C. S., et al. 2010, The Astrophysical Journal, 721, 1014

MacLeod, C. L., Brooks, K., Ivezić, Ž., et al. 2011, The Astrophysical Journal, 728, 26

MacLeod, C. L., Ivezić, Ž., Sesar, B., et al. 2012, The Astrophysical Journal, 753, 106

McGreer, I. D., Fan, X., Jiang, L., & Cai, Z. 2018, AJ, 155, 131, doi: 10.3847/1538-3881/aaaab4
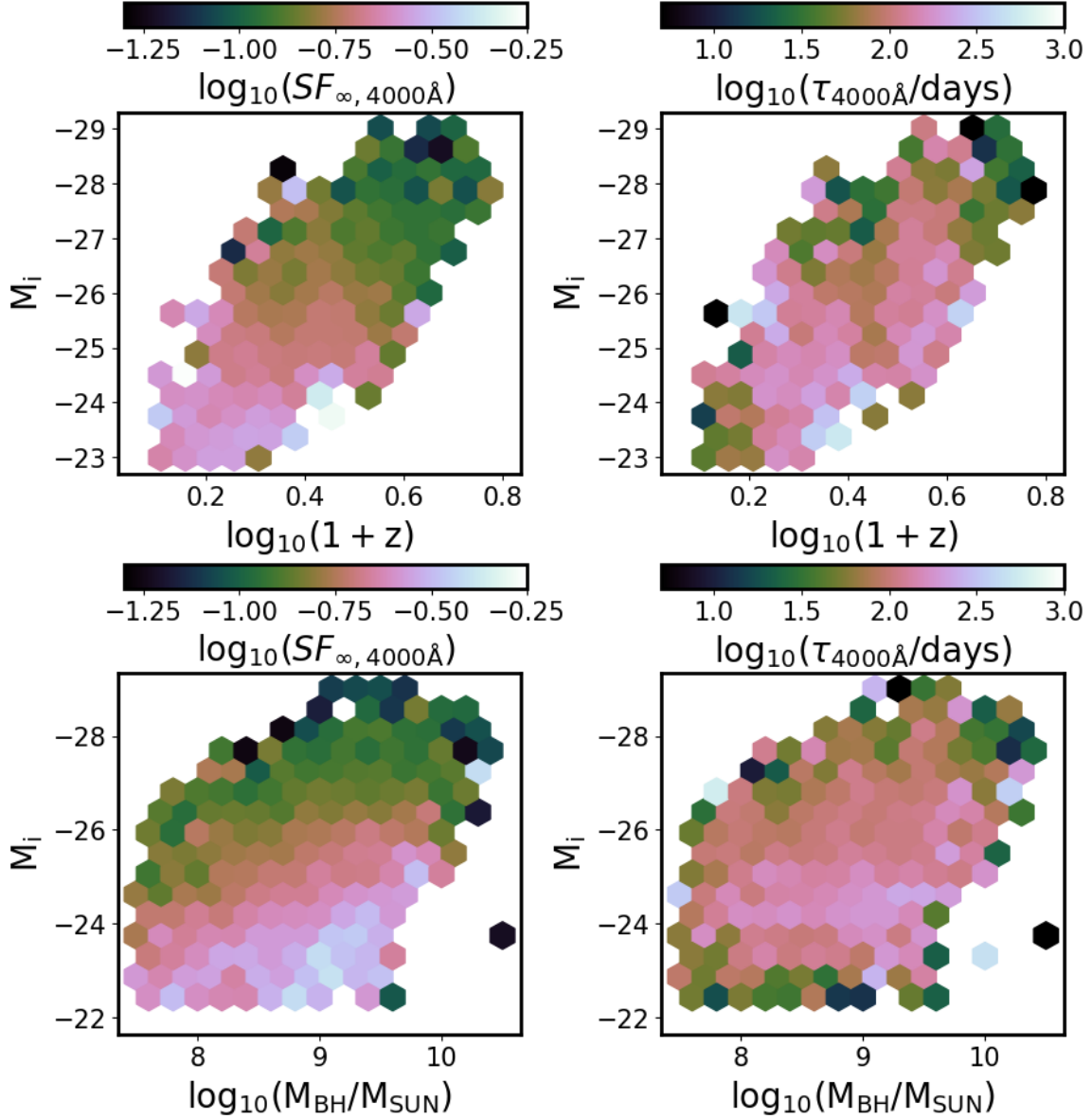
Figure 14. Long-term variability (SF_∞), and characteristic timescale (τ), as a function of absolute i-band magnitude (K-corrected to redshift 2, proxy for bolometric luminosity), virial black hole mass, and redshift.

McGreer, I. D., Jiang, L., Fan, X., et al. 2013, ApJ, 768, 105, doi: 10.1088/0004-637X/768/2/105

Oke, J. B., & Sandage, A. 1968, ApJ, 154, 21, doi: 10.1086/149737

Palanque-Delabrouille, N., Magneville, C., Yèche, C., et al. 2013, A&A, 551, A29, doi: 10.1051/0004-6361/201220379

Pâris, I., Petitjean, P., Ross, N. P., et al. 2017, A&A, 597, A79, doi: 10.1051/0004-6361/201527999

Pâris, I., Petitjean, P., Aubourg, É., et al. 2018, A&A, 613, A51, doi: 10.1051/0004-6361/201732445

Rau, A., Kulkarni, S. R., Law, N. M., et al. 2009, PASP, 121, 1334, doi: 10.1086/605911

Richards, G. T., Strauss, M. A., Fan, X., et al. 2006, AJ, 131, 2766, doi: 10.1086/503559

Ross, N. P., McGreer, I. D., White, M., et al. 2013, ApJ, 773, doi: 10.1088/0004-637X/773/1/14

Rybicki, G. B., & Press, W. H. 1992, ApJ, 398, 169, doi: 10.1086/171845

Sánchez-Sáez, P., Lira, P., Mejía-Restrepo, J., et al. 2018, ApJ, 864, 87, doi: 10.3847/1538-4357/aad7f9

Schneider, D. P., Hall, P. B., Richards, G. T., et al. 2007, AJ, 134, 102, doi: 10.1086/518474

—. 2008, VizieR Online Data Catalog, 7252

Schneider, D. P., Richards, G. T., Hall, P. B., et al. 2010, AJ, 139, 2360, doi: 10.1088/0004-6256/139/6/2360
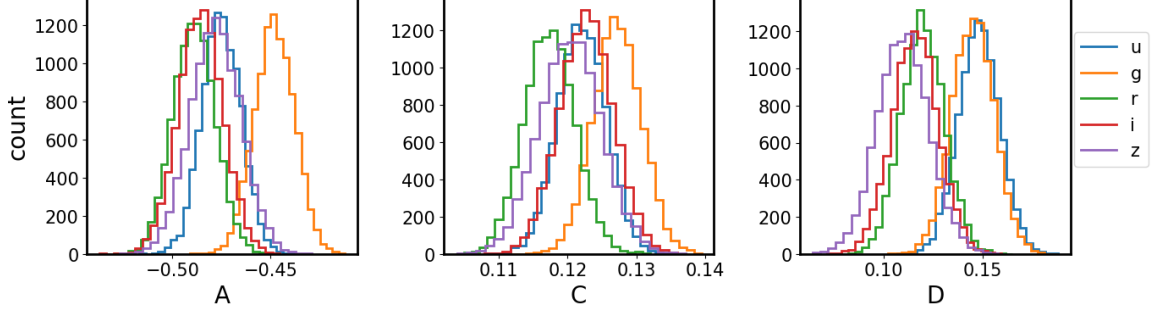
Figure 15. Table 1 in M10 reported the band-averaged values for fit coefficients A,C,D for Eq. 16. Shown here are samples from posterior MCMC draws using M10 results for $f = SF_\infty$, against Shen et al. 2011 M_i and M_{BH}. Because the SDSS r-band results are different from band-averaged values, we compare our SDSS-PS1 combined r-band results against M10 SDSS r-band only.
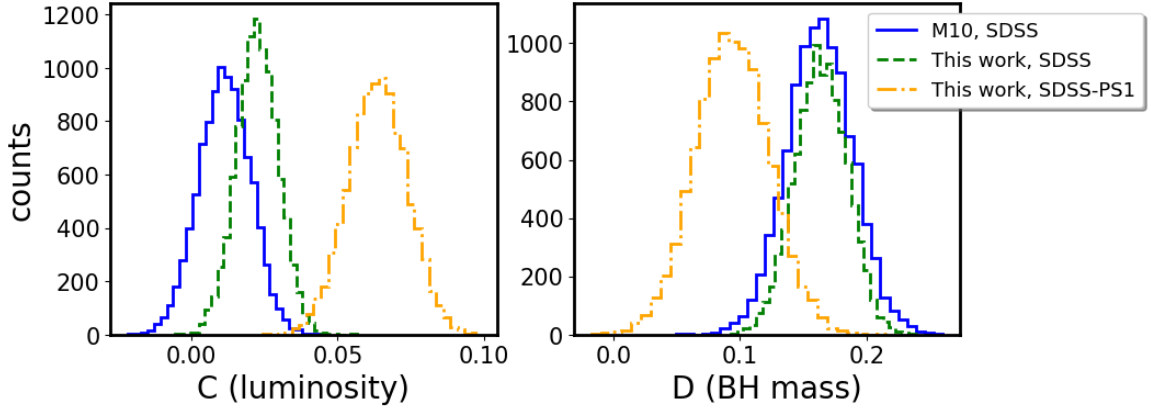

Figure 16. Comparison of our fits to Eq. 16, for $f = \tau$ with SDSS only, or SDSS-PS1 combined quasar light curves, against M10 SDSS r-band. The results from SDSS-only portion are consistent with M10 for the single band. Inclusion of the PS1 portion decreases the timescale dependence on black hole mass, but increases the luminosity dependence. This can be understood as a rotation of the plane in (τ, M_i, M_{BH}) coordinates.
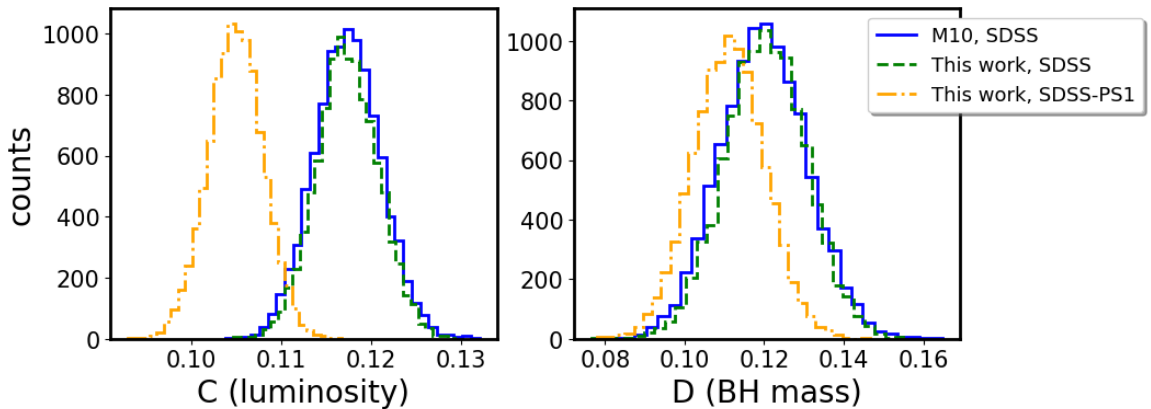

Figure 17. Same as Fig. 16, but fitting quasar absolute magnitude, and black hole mass in Eq. 16 as a function of the asymptotic amplitude $f = SF_\infty$. New data from PS1 supports a weaker dependence of variability amplitude with luminosity and black hole mass.

Table 1. Color terms (offsets) between the following survey filters and SDSS(r) band, using the mean SDSS(g-i) color, so that the synthetic SDSS(r) magnitude can be found as $r_{SDSS,synth} = x - B_0 - B_1 SDSS(g-i)$

Band (x)	B_0	B_1
CRTS V	-0.0464	-0.0128
PTF g	-0.0294	0.6404
PTF R	0.0058	-0.1019
PS1 g	0.0194	0.6207
PS1 r	0.0057	-0.0014
PS1 i	0.0247	-0.2765

NOTE—To derive the offsets we used SDSS S82 1 mln standard stars catalog (Ivezić et al. 2007). We randomly selected 10% of that catalog, for which 48250 have CRTS light curves with at least 10 observations (B.Sesar). For these stars we obtained PS1 photometry from MAST http://panstarrs.stsci.edu and PTF from IRSA PTF Object Catalog https://irsa.ipac.caltech.edu/. We further imposed quality cuts requiring that the stars are bright: $r < 19$.

Sesar, B., Ivezić, Ž., Lupton, R. H., et al. 2007, AJ, 134, 2236

Shen, Y., Greene, J. E., Strauss, M. A., Richards, G. T., & Schneider, D. P. 2008, ApJ, 680, 169, doi: 10.1086/587475

Shen, Y., Richards, G. T., Strauss, M. A., et al. 2011, ApJS, 194, 45, doi: 10.1088/0067-0049/194/2/45

Shen, Y., Hall, P. B., Horne, K., et al. 2018, arXiv e-prints, arXiv:1810.01447. https://arxiv.org/abs/1810.01447

Sun, M., Xue, Y., Wang, J., Cai, Z., & Guo, H. 2018, ApJ, 866, 74, doi: 10.3847/1538-4357/aae208

Tonry, J. L., Stubbs, C. W., Lykke, K. R., et al. 2012, ApJ, 750, 99, doi: 10.1088/0004-637X/750/2/99

Vanden Berk, D. E., Richards, G. T., Bauer, A., et al. 2001, AJ, 122, 549, doi: 10.1086/321167

Vestergaard, M. 2002, ApJ, 571, 733, doi: 10.1086/340045

Vestergaard, M., & Peterson, B. M. 2006, ApJ, 641, 689, doi: 10.1086/500572

Wisotzki, L. 2000, A&A, 353, 861

Yang, J., Fan, X., Wu, X.-B., et al. 2017, AJ, 153, 184, doi: 10.3847/1538-3881/aa6577

Zu, Y., Kochanek, C. S., Kozłowski, S., & Udalski, A. 2013, ApJ, 765, 106, doi: 10.1088/0004-637X/765/2/106

Zu, Y., Kochanek, C. S., & Peterson, B. M. 2011, ApJ, 735, 80